Feature-Driven Multilayer Visualization for Remotely Sensed Hyperspectral Imagery

Shangshu Cai, *Member, IEEE*, Qian Du, *Senior Member, IEEE*, and Robert J. Moorhead, II, *Senior Member, IEEE*

***Abstract*—Displaying the abundant information contained in a remotely sensed hyperspectral image is a challenging problem. Currently, no approach can satisfactorily render the desired information at arbitrary levels of detail. In this paper, we present a feature-driven multilayer visualization technique that automatically chooses data visualization techniques based on the spatial distribution and importance of the endmembers. It can simultaneously visualize the overall material distribution, subpixel level details, and target pixels and materials. By incorporating interactive tools, different levels of detail can be presented per users' request. This scheme employs five layers from the bottom to the top: the background layer, data-driven spot layer, pie-chart layer, oriented sliver layer, and anomaly layer. The background layer provides the basic tone of the display; the data-driven spot layer manifests the overall material distribution in an image scene; the pie-chart layer presents the precise abundances of endmember materials in each pixel; the oriented sliver layer emphasizes the distribution of important anomalous materials; and the anomaly layer highlights anomaly pixels (i.e., potential targets). Displays of the airborne AVIRIS data and spaceborne Hyperion data demonstrate that the proposed multilayer visualization scheme can efficiently display more information globally and locally.**

***Index Terms*—Hyperspectral image visualization, mixed-pixel visualization, multilayer visualization.**

I. Introduction

A HYPERSPECTRAL imaging sensor collects data with hundreds of contiguous and narrow spectral bands. Its high spectral resolution permits more accurate detection, classification, identification, and quantification. However, visualization of the information contained in such a huge data volume is a challenge. Displaying high-dimensional data in a single image results in information loss. Our goal is to visualize information and to enhance data features as much as possible.

Visualization has been part of remote sensing for decades, beginning with false-color display. For example, the typical way of displaying multispectral data is a color infrared (CIR) composite, which maps the near-infrared, red, and green bands to the RGB channels. It provides a synoptic overview of the scene, where vegetation can be effectively visualized in red [1]. Robertson *et al.* mapped an original multispectral image into a perceptual uniform color space to generate a color image with high contrast [2]. Due to the low signal-to-noise ratio (SNR) of remotely sensed images, Durand *et al.* selected three bands and enhanced color contrast by balancing the SNR of the three bands [3]. Demir *et al.* proposed a low complexity hyperspectral visualization scheme that used one-bit-transformation-based band selection to preserve the maximum information contained in the original imagery [4]. When these algorithms are used to display hyperspectral imagery, they may not be sufficient because they cannot handle the large amount of information contained in hundreds of spectral channels.

Compacting the information in a hyperspectral image for display is another common approach. For instance, Principal Component Analysis (PCA) condenses the information in hundreds of bands into major principal components (PCs) and then displays the PCs in a color image. Tyo *et al.* employed PCA to display hyperspectral images by mapping the first three PCs to the hue–saturation–value (HSV) color space [5]. Segmented PCA was used to visualize and classify hyperspectral imagery in [6]. However, PCA-based methods do not balance the SNR well. Noise may dominate some PCs, which results in a higher-ranking PC containing less signal information than a lower-ranking PC. Therefore, a noise-adjusted principal component analysis (NAPCA) may be a better choice [7]. A PCA-class method for hyperspectral image color display was studied in [8], [9]. In general, these unsupervised transformation techniques still result in great loss of useful information.

Jacobson *et al.* [10], [11] visualized hyperspectral images by fixing a linear spectral weight for each channel or adjusting the weights with the SNR. In this way, the same material in different data sets can be visualized in a similar color. An interactive visualization approach using convex optimization was introduced to visualize hyperspectral imagery by Cui *et al.* [12]. However, these approaches visualize all the information in one image and do not help observers distinguish different materials, which may be easily separated in the original data due to its high dimensionality.

Another way to display hyperspectral images is to visualize the classification results. For hard classification, a distinctive visual representation could be formed by assigning a color label to each class [13]. This approach, however, eliminates the mixture information in hyperspectral pixels. Due to the relative low spatial resolution, the signature of each pixel normally consists of the signatures of different materials. It is more

Manuscript received March 3, 2009; revised August 22, 2009 and February 16, 2010. Date of publication May 10, 2010; date of current version August 25, 2010. This work was supported by the NASA Science Mission Directorate, Earth System Division, Applied Sciences Program as part of a Crosscutting Solutions contract to Mississippi State University through Stennis Space Center.

S. Cai is with the Center for Risk Studies and Safety, University of California Santa Barbara, Goleta, CA 93117 USA.

Q. Du and R. J. Moorhead, II are with the Department of Electrical and Computer Engineering and Geosystems Research Institute, High Performance Computing Collaboratory, Mississippi State University, Mississippi State, MS 39762 USA.

Color versions of one or more of the figures in this paper are available online at http://ieeexplore.ieee.org.

Digital Object Identifier 10.1109/TGRS.2010.2047021

appropriate to conduct mixed-pixel classification, where a pixel is classified according to the percentage of each material present [14], [15]. Traditionally, these mixed classification results are displayed as grayscale images separately and viewed side-by-side. This makes it difficult to reveal the spatial relationship among classes. Wessels *et al.* tried to solve this problem by displaying them in a single image [16]. In their work, the pixel color chosen was the one assigned to the most abundant material resident in that pixel area, unfortunately suppressing the abundances from other materials.

It should be noted that the display of classification results can be considered a multivariate visualization problem. This problem has been studied for many years. In [17], multiple flow variables were mapped to different visual elements and multiple fields were presented on a surface successfully. Forsell *et al.* employed texture and 3-D surface shape to display multivariate data simultaneously [18]. Bokinsky showed that different sizes and distributions of dots could successfully represent different variables [19]. Multiple scalar fields have been visualized by textured splats [20], oriented texture slivers [21], [22], synthesized cell texture (SCT) [23], and hue and oriented texture [24], [25]. In Urness's work, multiple collocated flow fields and scalar variables were displayed using texture, glyph, and color [26]. All of these methods only qualitatively visualize the collocated multiple vector or scalar fields, and cannot indicate the quantitative information precisely. In addition, they consider the multivariate data as independent quantities and do not show the relationship between variables.

Previously, we presented a new approach for the visualization of hyperspectral imagery that employed a pie-chart layer to visualize the mixed-pixel information [27]. This approach takes advantage of the classification result from fully constrained linear unmixing such as the technique in [14]. At the very detailed level, it displays pixel composition at the subpixel level. On the other hand, it is able to display the overall material distribution in an image scene. Viewers can choose any detail level for information display. However, this approach has some limitations. Since the double-layer scheme employed color combination to display the overall distribution, new colors could be generated by the color mixing processing and mislead the observers. The statistical distribution of a specific material within a certain area is difficult to know. Quick decision-making on targets with low occurrence probability may be impossible without zooming into them and reading many pie-charts. To provide more information with better visibility both globally and locally, the pie-chart layer needs to be improved and integrated with other existing multivariate visualization methods.

This paper is organized as follows. Section II briefly describes the linear mixture analysis of hyperspectral imagery and presents the mixed-pixel classification that can be achieved; Section III reviews several existing techniques that can be applied to hyperspectral image visualization and discusses their limitations; Section IV proposes a new multilayer visualization technique that overcomes those limitations; Section V presents an additional example using Hyperion data; Section VI evaluates the presented approaches by subject tests; and Section VII gives the conclusion.

II. Linear Mixture Model

In a remotely sensed image, the reflectance of each pixel is considered as the mixture of the reflectance from distinctive materials residing in an image scene. These materials are referred to as *endmembers*. The linear mixture model (LMM) assumes the mixture mechanism is linear and is widely used to analyze hyperspectral imagery [14], [15], [28], [29].

Let $\mathbf{r}$ denote a pixel vector with dimensionality L, where L is the number of spectral bands. Assume the number of endmember materials is p. Let $\mathbf{M}$ be the signature matrix of these materials denoted as $\mathbf{M} = [\mathbf{m}_1, \ldots, \mathbf{m}_k, \ldots, \mathbf{m}_p]$, where $\mathbf{m}_k$ is the signature of the kth endmember material. According to the LMM, a pixel vector $\mathbf{r}$ can be represented as

$$\mathbf{r} = \mathbf{M}\boldsymbol{\alpha} + \mathbf{n} \tag{1}$$

where $\boldsymbol{\alpha} = (\alpha_1, \ldots, \alpha_k, \ldots, \alpha_p)^T$ is a $p \times 1$ abundance vector, whose kth element α_k represents the proportion of the kth endmember $\mathbf{m}_k$ present in $\mathbf{r}$. Here, $\mathbf{n}$ accommodates additive noise or sensor measurement error.

Since a α represents endmember abundance, it should be a nonnegative value. Also, the whole pixel is constructed by all the endmembers. Hence, their sum should be one. These two constraints can be expressed as

$$\sum_{k=1}^{p} \alpha_k = 1 \quad \text{and} \quad 0 \le \alpha_k \le 1. \tag{2}$$

A constrained optimization problem can be formulated to estimate the $\boldsymbol{\alpha}$ that yields the minimum error in pixel reconstruction while the constraints in (2) are satisfied. This is referred to as a fully constrained least squares linear unmixing (FCLSLU) problem. If $\mathbf{M}$ is known, it can be easily achieved via quadratic programming. If $\mathbf{M}$ is unknown, then an unsupervised FCLSLU algorithm needs to be performed [14]. The procedure in FCLSLU can be described as follows.

- Step 1) Select the two pixels with the maximum and minimum norm from the image and construct the initial endmember signature matrix $\hat{\mathbf{M}} = [\mathbf{m}_1, \mathbf{m}_2]$. Then, use quadratic programming to estimate $\hat{\boldsymbol{\alpha}} = (\hat{\alpha}_1 \hat{\alpha}_2)^T$.
- Step 2) Calculate the reconstruction error, e, between the pixel vector $\mathbf{r}$ and its estimate, i.e., $e = \|\mathbf{r} - \hat{\mathbf{M}}\hat{\boldsymbol{\alpha}}\|$.
- Step 3) Find the pixel that has the maximum error and take it as a third endmember, i.e., $\hat{\mathbf{M}} = [\mathbf{m}_1, \mathbf{m}_2, \mathbf{m}_3]$. This is done because this pixel is considered as the most dissimilar pixel from $\mathbf{m}_1$ and $\mathbf{m}_2$.
- Step 4) Repeat Steps 2) and 3) for additional endmembers until the maximum error is less than a given threshold ξ or the maximum number of endmembers is reached.

When the number of endmembers is unknown, a large number can be assumed first to run the unsupervised FCLSLU algorithm. Then, similar endmember signatures can be combined using a spectral angle mapper (SAM) [30], and the endmember signatures corresponding to noisy abundance images with large entropies can be removed. The remaining signatures are used for the supervised FCLSLU to generate the final abundance images for visualization.

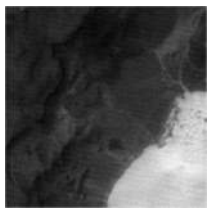

Fig. 1. AVIRIS Lunar Lake scene of size 200 × 200.

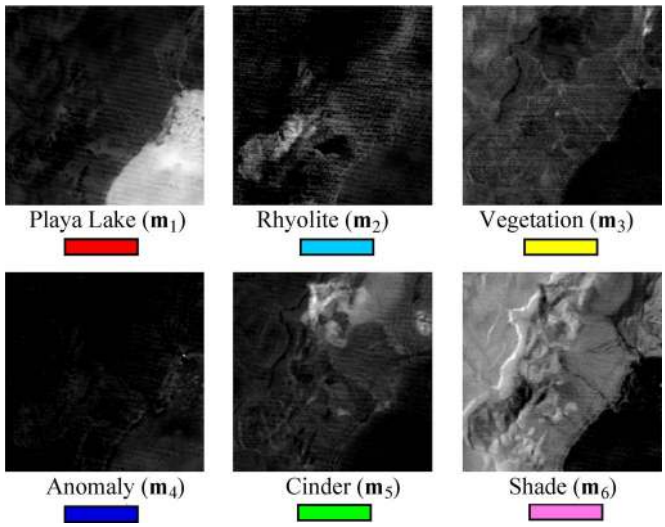

Fig. 2. Abundance images of the AVIRIS Lunar Lake scene.

The Lunar Lake data taken by Airborne Visible/InfraRed Imaging Spectrometer (AVIRIS) was used in this study. The subscene of size 200 × 200 in Fig. 1 was classified by the unsupervised FCLSLU algorithm. Fig. 2 shows the abundance images of the six materials, namely, {Playa Lake, Rhyolite, Vegetation, Anomaly, Cinder, and shade} based on some prior information [31]. In a grayscale abundance image, a dark pixel represents low abundance of the corresponding material.

III. Visualization Techniques for Hyperspectral Imagery

The major disadvantage of viewing the grayscale abundance images side-by-side is the difficulty of perceiving the spatial relationship between materials. Displaying them in a single image offers several advantages. For instance, the overall spatial distribution of materials can be easily presented, and it is possible to show the detailed pixel composition. In this section, we review the existing multivariate visualization techniques such as color combination, double-layer display, oriented slivers, and data-driven spots (DDS). Their pros and cons for hyperspectral image visualization are then discussed.

A. Color Representation of Hard Classification

The abundance images are converted into binary images using the following criterion:

$$\alpha_k = \begin{cases} 1, & \text{if } \alpha_k \text{ is the maximum in } \boldsymbol{\alpha} \\ 0, & \text{otherwise.} \end{cases} \tag{3}$$

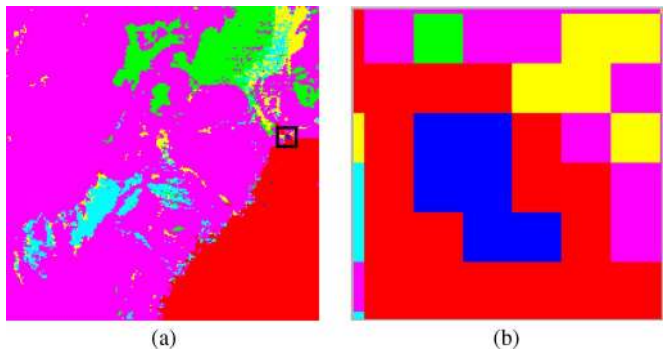

Fig. 3. Color representation of hard classification. (a) Overall display. (b) Zoomed-in display for the ROI highlighted in (a).

Then, the resulting hard classification maps can be displayed in a single color image. Fig. 3(a) shows the color composite after the abundance images in Fig. 2 are converted into binary and combined into one image. Fig. 3(b) shows the color display of a region of interest (ROI), including the anomaly marked in Fig. 3(a). Obviously, the mixed-pixel information is lost.

B. Color Combination Result

Because the hard classification loses mixed-pixel information, a color assignment scheme that depends on the abundances of each endmember should be applied. Let the color vector assigned to the kth endmember be $\mathbf{c}_k = (r_k, g_k, b_k)^T$. Then, a color matrix can be formed as

$$\mathbf{C} = [\mathbf{c}_1, \ldots, \mathbf{c}_k, \ldots, \mathbf{c}_p] = \begin{bmatrix} r_1 & \cdots & r_k & \cdots & r_p \\ g_1 & \cdots & g_k & \cdots & g_p \\ b_1 & \cdots & b_k & \cdots & b_p \end{bmatrix}. \tag{4}$$

The final color $\mathbf{c}(i,j)$ for a pixel $\mathbf{r}_{ij}$ with abundance vector $\boldsymbol{\alpha}(i,j)$ is

$$\mathbf{c}(i,j) = \mathbf{C}\boldsymbol{\alpha}(i,j). \tag{5}$$

Because the final color for each pixel is the linear combination of the colors assigned to endmembers, the final color is a function of the endmember abundances. Compared to the color representation of hard classification, Fig. 4(a) displays not only the spatial location of each endmember, but also the distribution variations. As shown in Fig. 4(b), the small ROI has greater variations than shown in Fig. 3(b). However, it is difficult to predict the final color appearance due to the nonlinear nature of color perception.

C. Double-Layer Visualization

In addition to the general material distribution, the detailed composition of each pixel may be of interest in many cases. The double-layer visualization was proposed for this purpose [27]. It employs the color representation as a background layer and a pie-chart layer as a foreground layer.

In a pie-chart, each endmember is assigned to a fan-shaped region (shown as Fig. 5). Without loss of generality, the first endmember is assigned to the first region, the second endmember to the second region, and so on. The area of the fan-shaped

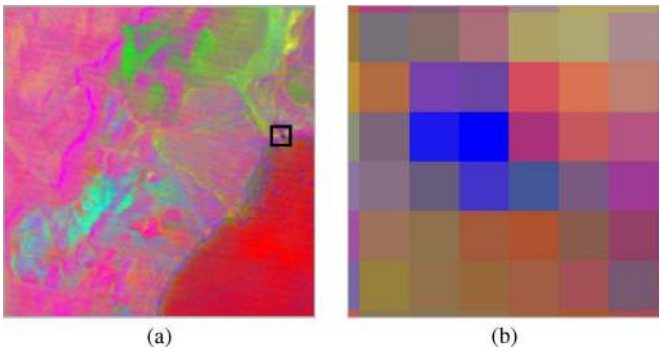

Fig. 4. Color representation of soft classification. (a) Overall display. (b) Zoomed-in display for the ROI highlighted in (a).

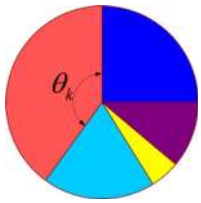

Fig. 5. Fan-shaped superpxiel with its mixture composition.

region for the kth endmember is proportional to the angle θ_k, which is determined by its abundance α_k, i.e.,

$$\theta_k = \alpha_k \cdot 360^\circ. \tag{6}$$

Its starting and ending positions can be represented, respectively, as

$$\beta_k^s = \sum_{j=1}^{k-1} \theta_j \quad \text{and} \quad \beta_k^e = \sum_{j=1}^{k} \theta_j. \tag{7}$$

They can be related by $\theta_k = \beta_k^e - \beta_k^s$, and $\beta_1^s = 0^\circ$.

Because $\boldsymbol{\alpha}$ is constrained by (2), a pixel is shown as a full disk, i.e., $\beta_p^e = 360^\circ$.

Opacity is the parameter used to control the blending of these two layers. The opacity of the pie-charts in the foreground layer is associated with a zooming parameter automatically or manually. When the combined image is zoomed out to display the overall distribution, the opacity of the pie-charts is set to a low value; therefore, the background layer dominates the image, as shown in Fig. 6(a). If the opacity of the pie-chart layer is set to a high value when viewers zoom in for detail, then the pie-chart of each pixel pops out. Fig. 6(b) shows the ROI when the opacity is set to 1.0.

D. Oriented Slivers

Oriented slivers were employed to visualize multivariate data in [21] and [22]. The main idea of oriented slivers is that slivers with different slopes are used to represent different variables and the transparency of the slivers is controlled by the data value. The more visible a sliver is, the greater the value it represents.

To visualize a hyperspectral image pixel, a sliver is used to represent an endmember. In order to manifest the endmember

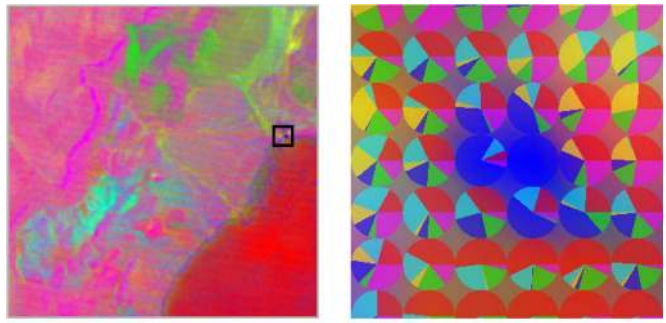

Fig. 6. Double-layer visualization. (a) Overall display. (b) Zoomed-in display for the ROI highlighted in (a).

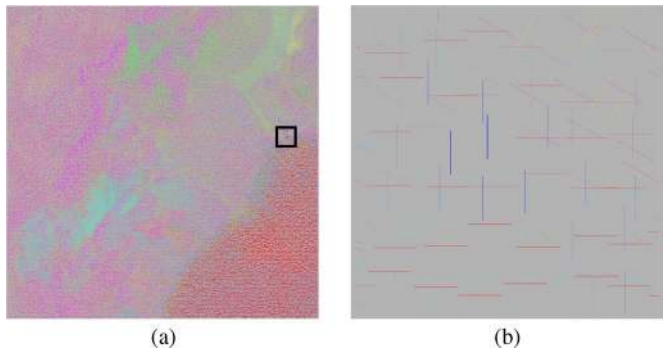

Fig. 7. Oriented sliver representation. (a) Overall display. (b) Zoomed-in display for the ROI highlighted in (a).

distribution, the color, orientation, and transparency of a sliver are encoded by the endmember type and its abundance in the corresponding pixel. As shown in Fig. 7(a), the overall distribution of endmembers is revealed by colors with different tone and saturation. Compared to Fig. 6(a), the blue material is more perceivable in the right bottom corner. In Fig. 7(b), the detailed information of endmembers in each pixel is shown. The primary endmember information is obvious, but other endmember information usually cannot be easily perceived.

E. Data-Driven Spots (DDS)

The DDS technique was introduced by Bokinsky [19] to visualize multiple collocated variables. The major idea is to map different variables such as cats, dogs, and chickens into Gaussian-shaped spots in different sublayers. Each variable occupies one sublayer. The quantity of a variable controls the transparency of a related spot in the corresponding sublayer. In each sublayer, spots are not displayed at every grid; instead, they are displayed at the sampled grid. Thus, information of lower sublayers can be read through the upper sublayers.

Fig. 8 shows the DDS visualization of the AVIRIS Lunar Lake scene, where colors are used to encode uniformly shaped spots representing different endmember materials. If a material is highly abundant in a certain area, then the number of spots with a specific color is large. The general distribution of endmembers is visible in Fig. 8(a) and the detailed distribution is shown in the ROI in Fig. 8(b). We can see that the spot transparency reflects the value of material abundance. If the

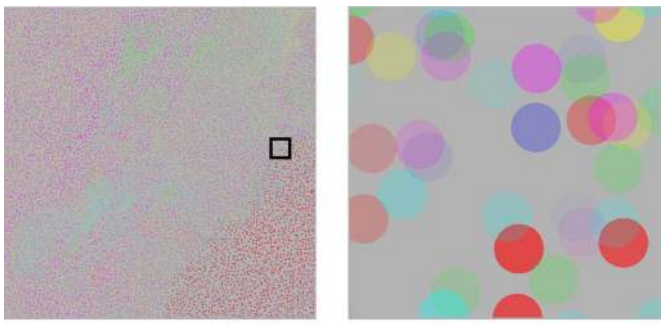

Fig. 8. DDS representation. (a) Overall display. (b) Zoomed-in display for the ROI highlighted in (a).

abundance is larger, the corresponding spot is more visible. Unfortunately, the anomaly in the ROI is missed in Fig. 8(a), which is due to the sampling process required for DDS visualization.

F. Discussion

The aforementioned techniques have certain capabilities to display the distribution of endmember materials in a hyperspectral image, but limitations need to be resolved mainly due to the importance of subpixel level analysis in hyperspectral imagery.

Hard classification obviously distorts the material distribution since it ignores the materials with smaller abundances, so it will not be used in this research. Color representation of mixed-pixel classification and DDS can display the overall distribution, but they cannot reveal the detailed information at subpixel level. In particular, the DDS representation reveals the statistical distribution, but it is prone to miss small targets. The oriented sliver representation can present both the overall distribution and part of the mixed-pixel information.

The pie-chart display visualizes the general distribution as background and the detail information as foreground. In some cases, it may be helpful if the visualized image can directly display the important mixed-pixel information without the need of zooming into each pie-chart. For instance, an anomaly is a pixel whose spectral signature is very different from the surrounding pixels and has low probability to appear as a potential target. If a visualization technique can assist in rapidly locating an anomaly in the mixed-pixel composition, it will greatly facilitate the decision-making. Obviously, two layers are not enough to meet the requirements. Therefore, a multilayer visualization technique is proposed in the next section.

IV. Multilayer Visualization

To overcome the limitations of each technique in Section III, a feature-driven multilayer visualization technique is proposed in this paper. This algorithm analyzes the spatial distribution and importance of each endmember and then assigns a proper visualization technique to visualize this endmember. This approach emphasizes the visibility of the anomalous and low-probability materials; at the same time, it adequately visualizes the widely distributed endmembers and the detailed distribution at the subpixel level.

A. Functions of Five Layers

Five layers are employed to maximize the information to be visualized. The five layers are, from bottom to top, the background layer, DDS layer, pie-chart layer, oriented sliver layers, and anomaly layers. Special considerations are needed to create the final display with acceptable texture. Each layer has a specific purpose as described below.

Background Layer: No information is presented by this layer. It is used to enhance the overall appearance of the display. Because it can be seen through the upper layers, the color in the background layer should be carefully chosen to make the final display more appealing. Neutral gray is chosen as suggested in [17] and [19].

DDS Layer: This layer displays the statistical distributions of the endmember materials that are widely distributed in the scene (i.e., background materials most likely). For an image with p materials, q sublayers $(q \leq p)$ are needed with one for each background material. Gaussian-shaped spots were recommended in the original DDS technique [19]. To make it suitable for multiple layer representation, solid circles are used with the radius equal to half of a pixel extent. Moreover, the uniform sampling in the original DDS technique is changed to non-uniform, which is more efficient in capturing subtle variations. Hence, the fact that spots with the same color are densely packed in a unit area means the corresponding material is more concentrated in this area. The opacity of a spot is controlled by the corresponding abundance in the sampled pixel it represents. In other words, if pixel $\mathbf{r}_{ij}$ is the sampled pixel for the spot at (i, j) in the kth DDS sublayer representing the kth endmember, the opacity $o_k(i, j)$ is determined as

$$o_k(i, j) = \alpha_k(i, j) \tag{8}$$

where $\alpha_k(i, j)$ is the abundance of $\mathbf{m}_k$ in pixel $\mathbf{r}_{ij}$.

Pie-Chart Layer: This layer is used to display the detailed composition of each sampled pixel. The opacity should be low when visualizing the overall distribution to reduce the line pattern artifacts. Medium or high opacity is more appropriate for the ROI visualization. In addition, the radius of the pie-charts has to be reduced from that used in [27] and distinct from that of the dots in the DDS layer to work effectively in the multiple layer situation. The overall opacity of the pie-chart layer is associated with a zooming parameter.

Oriented Sliver Layer: This layer is to represent anomalous materials (associated with anomalies or targets), which are not spatially well distributed. These materials cannot be well represented by the DDS layer because of their low occurrence probability. Thus oriented slivers are used to emphasize these materials as long as they are present in a pixel. Different materials are distinguished by orientation. The opacity of a sliver is controlled by the abundance of the anomalous endmember in the pixel.

Anomaly Layer: An anomaly is a potential target. The anomalous pixels should be significantly highlighted. In order to make the anomalies preattentive and distinguished from other materials, large 3-D icons with bright colors are employed in this layer to represent anomalies.

It should be noted that the colors assigned to endmembers in all layers (DDS, pie-chart, oriented slivers, and anomaly) are the same. Layer transparency/opacity can be automatically or manually adjusted.

B. Material Categorization

The anomalous endmembers are not widely distributed. Under an unsupervised situation, the category of endmember $\mathbf{m}_k$ can be determined by calculating the overall distribution index, I_k, defined as

$$I_k = \frac{M_k N_k}{N^2} \tag{9}$$

where M_k is the total distributed amount of endmember $\mathbf{m}_k$, i.e.,

$$M_k = \sum_{i,j} \alpha_k(i,j). \tag{10}$$

N_k is the total number of pixels whose maximum abundance is from $\mathbf{m}_k$, and N is the total number of pixels in the scene. If I_k is less than a threshold η_m, $\mathbf{m}_k$ is considered an anomalous endmember; otherwise, it is a non-anomalous endmember. η_m is set to be 1×10^{-3} in this study. An anomalous material will be emphasized by the oriented sliver layer, which can be a foreground material. For a pixel to be considered an anomaly and thus be highlighted in the anomaly layer, the abundance value should be greater than a threshold η_p. In this study, η_p is set to be 0.8–0.9. A non-anomalous endmember is widely distributed and is usually a background material. It will be displayed by the DSS layer.

C. Resampling

In Bokinsky's DDS technique [19], spot density is independent of the scalar field because uniform sampling is used. This makes any subtle variation in distribution unnoticeable. Therefore, non-uniform sampling is proposed in this research. The sampling process for the kth material represented by the kth sublayer has the following steps:

Step 1) Set two controlling parameters: D_1 and D_2. The initial sampled pixel set $\Omega = \varnothing$.

Step 2) Randomly choose a pixel $\mathbf{r}_{ij}$ from the image scene.

Step 3) Calculate the threshold η_D for $\mathbf{r}_{ij}$ as

$$\eta_D(i,j) = (1 - a_k(i,j))\,(D_1 - D_2) + D_2. \tag{11}$$

Step 4) Calculate the coordinate distance between $\mathbf{r}_{ij}$ and each pixel in Ω. If all the distances are greater than η_D, $\mathbf{r}_{ij}$ is added to the sample set Ω.

Step 5) Repeat Steps 2) through 4) until the number of iterations are sufficiently large, say, $0.5N$.

Here, D_1 and D_2 are the minimum distances allowed between two samples when $\alpha_k(i,j)$ takes the smallest (i.e., $\alpha_k(i,j) = 0$) and the largest value (i.e., $\alpha_k(i,j) = 1$), respectively. Together, they control the final spot density. In our experiments $D_1 = 5$ and $D_2 = 1$. Obviously, this sampling algorithm is well correlated with the local abundance of the kth material. Because the threshold in (11) is smaller for pixels with larger abundance, these pixels have a greater chance of being selected. Even if a pixel with very low abundance is selected, the opacity control in (8) makes it almost invisible.

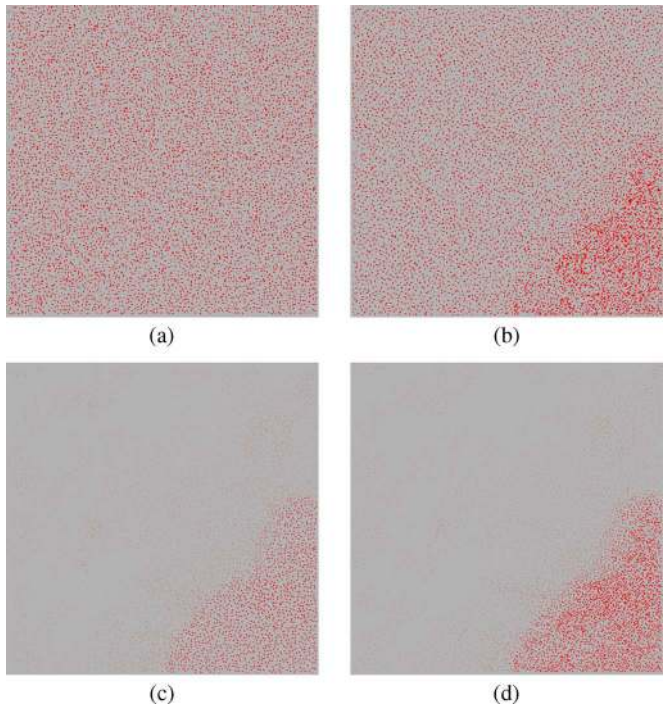

Fig. 9. Results of two sampling methods. (a) Uniform sampling. (b) Non-uniform sampling. (c) Uniform sampling after transparency control. (d) Non-uniform sampling after transparency control.

Fig. 9 shows the sampling results for Playa Lake (the 1st endmember material in Fig. 2). It is concentrated at the lower-right corner. Fig. 9(a) is the (original) uniform sampling result and Fig. 9(b) is the non-uniform sampling result where spots at the lower-right corner have higher density. After the transparency/opacity control using (8), Fig. 9(d) reflects the actual distribution variation of Playa Lake while Fig. 9(c) does not.

D. Layer Combination

After each layer has been generated, the final display is formed by alpha-blending, a standard computer graphics algorithm for semitransparent image display. By default, the blending parameter for the anomaly layer and background layer is 1.0, which means 100% opacity; those for the DDS layer and the oriented sliver layer are determined by the abundance value of a pixel (i,j); that for the pie-chart is associated with the zooming parameter. It should be noted that the sublayers in the DDS layer go through a similar blending process.

The final multilayer display for the AVIRIS Lunar Lake scene is shown in Fig. 10. Compared to the DSS display in Fig. 8(a), the overall display in Fig. 10(a) better manifests the variations of the six endmember materials; compared to the oriented sliver display in Fig. 7(a), the anomaly is more visible. Fig. 10(b) is the ROI with the anomaly layer; the precise location of the anomaly can be easily identified. Fig. 10(c)–(e) are the images when the opacity of the pie-chart layer is varied to increase the visibility of the detailed pixel information. In

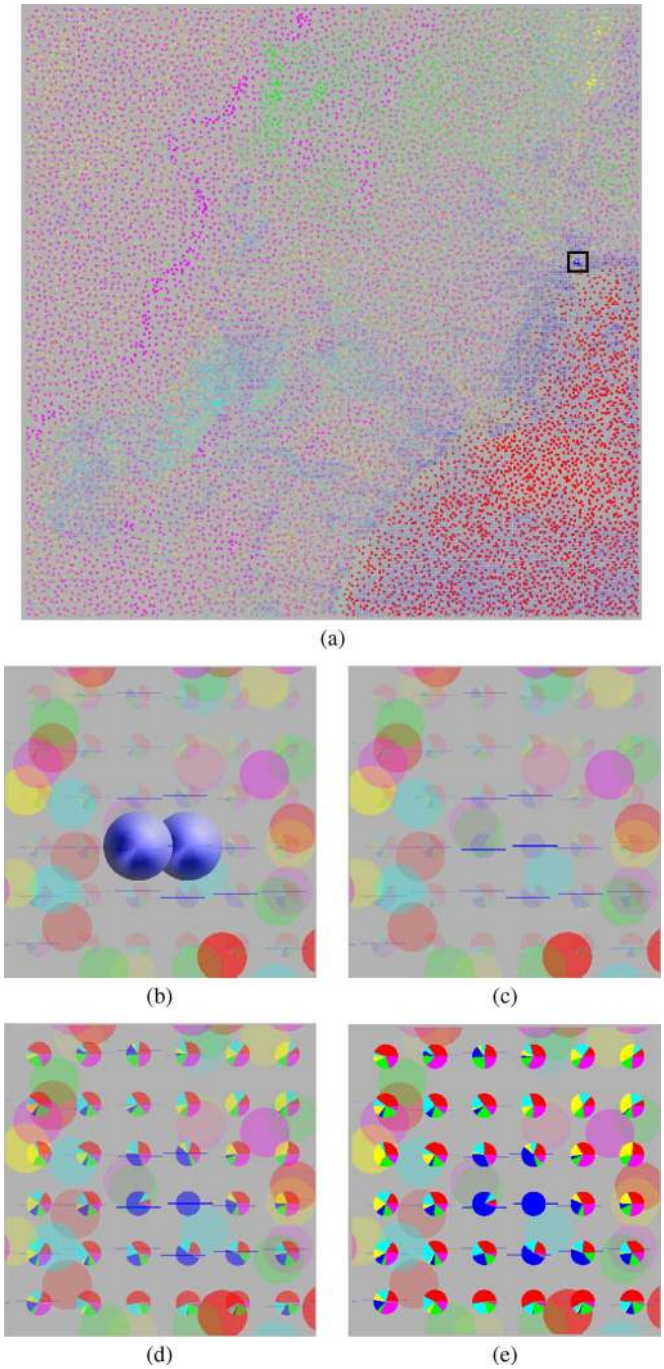

Fig. 10. Multilayer visualization of AVIRIS Lunar Lake. (a) Overall display with five layers. (b) ROI in the anomaly layer. (c)–(e) Displays with the opacity of the pie-chart layer being 0.1, 0.5, and 1.0, respectively (without the anomaly layer).

Fig. 10(c)–(e), the anomaly layer is deselected. We can also see the role of the oriented sliver layer, which is to make the pixels with the anomalous materials be more easily detected.

V. Hyperion Example

A Hyperion data set was used to verify the proposed multilayer algorithm. As the first spaceborne hyperspectral sensor, Hyperion images contain lots of sensor noise such as dark lines as shown in Fig. 11. The same preprocessing steps used in [27]

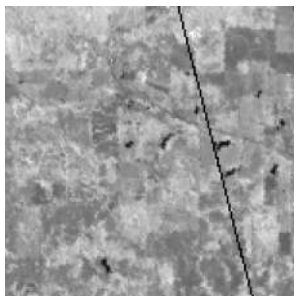

Fig. 11. Hyperion image scene of size 150 × 150.

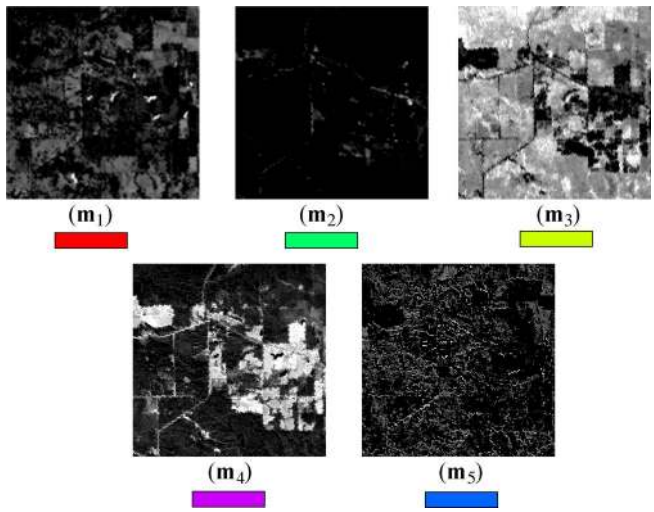

Fig. 12. Five abundance images of the Hyperion data.

were employed to remove the water absorption and noisy bands. 152 out of 220 bands were left for linear mixture analysis. Five abundance images were generated by the FCLSLU algorithms and color labels were automatically assigned. These are shown in Fig. 12.

According to the criterion in Section IV-B, materials 2 and 5 are considered as anomalous target materials while the other three materials are considered as widely distributed background materials. Several pixels were determined to be anomalies and are shown in green and blue depending on the material. Fig. 13 shows the multilayer display with and without the anomaly layer. When the anomaly layer was deployed as in Fig. 13(a), the anomalies could be more easily identified (in the areas marked with boxes). The DDS layer effectively visualized the three background materials in red, yellow, and purple, respectively. For instance, the locally concentrated red material was appropriately sampled and displayed. The sampled spots of the yellow and purple materials accurately reflected the actual distributions of these two materials.

Fig. 14 is a higher resolution rendering of the ROI indicated by the red box in Fig. 13. Fig. 14(a) contains the anomaly layer that pinpoints the locations of the anomalies, which are highlighted by the 3-D icons. When the anomaly layer is not shown, as in Fig. 14(b), we can see via the oriented sliver layer that neighboring pixels contain these two anomalous materials. Fig. 14(c)–(f) shows the data at various levels of transparency of the pie-chart layer. When the details of pixel

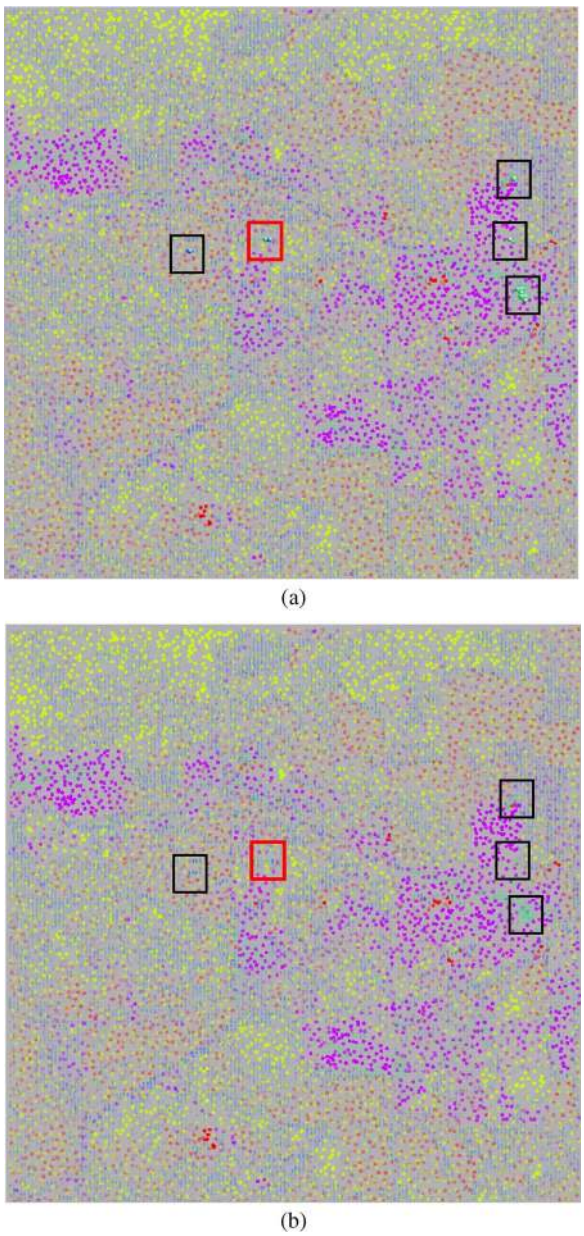

Fig. 13. Multilayer visualization for the Hyperion data set (a) with the anomaly layer and (b) without the anomaly layer.

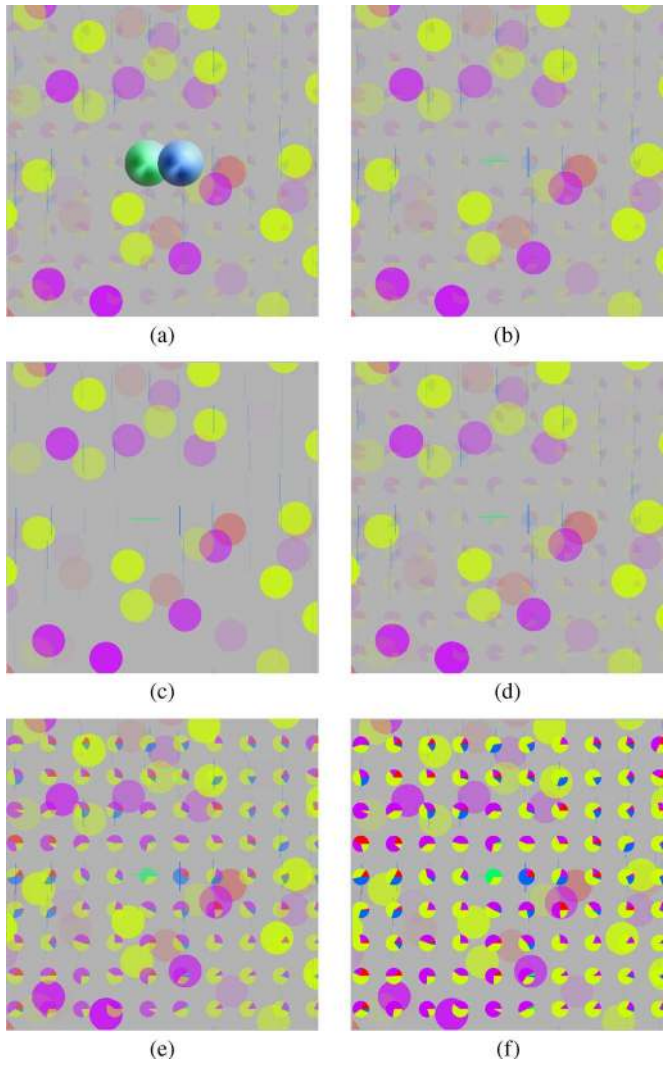

Fig. 14. Zoomed-in results of the ROI highlighted in the red box in Fig. 13. (a) With the anomaly layer and (b) without the anomaly layer. (c)–(f) Displays with the transparency of the pie-chart layer being changed from 0.0 (completely transparent), 0.1, 0.5, to 1.0 (completely opaque).

composition are not needed, the pie charts are made completely transparent as in Fig. 14(c). When the pixel composition needs to be studied, this layer can be made completely opaque as in Fig. 14(f). To prevent the DSS layer and oriented sliver layer from interfering with the analysis, these layers can be made completely transparent as well. As described in [27], a window can be popped up which lists the quantified abundances in each pixel.

VI. Evaluation and Discussion

Objective assessment is widely used to evaluate the multispectral/hyperspectral image fusion and compression. For instance, perceptual color distance [9], correlation coefficient [4], distance preservation and feature separability [12], and spectral angle preservation [10] were found to measure the fusion results. The Kullback–Leibler (KL) divergence was employed to assess the information content in color images [34]. Toet *et al.* extended a universal grayscale image quality index to a perceptually decorrelated color space to measure color image fidelity [33]. A broad range of perceptual quality metrics and their applications to still image compression have been reviewed by Eckert *et al.* [32]. However, these metrics cannot be directly used to validate the proposed approach since it is a feature-based visualization.

One of the objectives of hyperspectral image visualization is to help observers analyze the scene. For instance, if different classes are displayed distinctively, then classification can be accomplished more easily and accurately. Therefore, subjective measurement is employed to validate the presented visualization methods based on practical objectives. Subjective evaluation is widely used to study the pros and cons of visualization [38]. Bair *et al.* conducted a user study to find the optimal viewing for layered texture surfaces [35]. Acevedo *et al.* employed subjective evaluation to investigate how the perceptual interactions among visual elements impact the efficiency of

data exploration [36]. Ward and Theroux identified three phases of a user study: defining goals, creating data sets, and performing studies [37]. Cai *et al.* designed a user study to evaluate the layered visualization scheme for visualizing hyperspectral images [39].

In our subjective evaluation, five remote sensing researchers who have been analyzing hyperspectral images for several years were asked to evaluate the proposed method and other approaches. In order to reduce the environment impacts, the study was conducted in a laboratory on a 14-in Dell laptop computer with a screen resolution of 1400 $\times$ 1050. The luminance in the lab was constant during all the tests. Different visualization results were displayed to the researchers. They were asked to score the results using a five-level scoring system, in which 5 is the best and 1 is the worst. The answers were automatically recorded and the averages were calculated. Everyone was given the same amount of time, i.e., 20 min, to complete the entire assessment. Two real data sets discussed before were also used in this study: AVIRIS lunar lake and Hyperion data. The multilayer visualization technique was compared with hard classification (HARD), soft classification with color combination, double-layer scheme, OS, and DDS through the following five tasks:

Task 1—Subtle Variation (SV): This task compared the capability of the DDS and non-uniformed DDS in displaying a subtle variation of material spatial distribution. An endmember abundance map generated by FCLSLU was displayed first. Then, two displays were shown side-by-side: one visualized the endmember distribution by DDS and the other visualized by non-uniformed DDS. The question was: "Two visualization techniques are used to visualize the endmember distribution map. Which one do you think represents the variation better? Please mark it." All the observers thought non-uniformed DDS was better than DDS in manifesting the subtle variation.

Task 2—Anomaly Pixel Detection (APD): This task verified the capability of different techniques in helping observers find and detect the number of anomalous pixels. The question was: "In the following images, different visualization techniques are used to visualize classification result, i.e., the gray-scale abundance maps. Please indicate the number of anomalous pixels you can find in the area enclosed by the box." After the viewer clicked the answer, the right solution was displayed. Then, another another task was given: "Please score the visualization techniques based on the difficulty in finding actual anomalous pixels." According to the answers, the multilayer visualization technique could greatly facilitate anomalous pixel identification, yielding more accurate results.

Task 3—Endmember Number Estimation (ENS): This task tested the ability of visualization techniques in helping viewers extract different classes in a region of interest. The first task was: "Please indicate the number of different materials you can find in the area enclosed by the box." After the answer was given, the right solution was provided. Then, the viewer was given another task: "Please score the visualization techniques based on the difficulty in determining the actual number of endmembers." Although viewers could answer the first question quickly using HARD, the answers were often wrong. Thus, all of them gave HARD low scores. The average of the difficulty indicated that multilayer visualization could easily find the right answer.

TABLE I
EVALUATION OF VISUALIZATION TECHNIQUES

	APD	ENS	DIE	OA
HARD	2.2	2.2	2.0	1.9
Color Combination	3.1	3.0	2.8	3.1
Double Layer	3.1	3.0	4.7	3.6
OS	2.8	3.6	4.0	3.4
DDS	2.3	3.7	2.8	2.4
Multi-layer	4.5	4.0	4.6	3.4

Task 4—Detailed Information Extraction (DIE): This task validated the effectiveness of delivering detailed composition information at the subpixel level, including the number of endmembers and their percentages within the pixels. A cropped region of interest was displayed to viewers. For the central pixel in the region, the viewer was asked: "Please determine the number of endmembers and the range of the maximum abundance among all the endmember abundances." After the answers were provided, the solutions were shown. Then, another task was given: "Please score the visualization techniques based on the difficulty of extracting detailed information at the subpixel level." On average, viewers gave the double-layer and multilayer visualization schemes higher scores than the others.

Task 5—Overall Appearance (OA): This task found the viewers' opinion in the overall performance of the visualization techniques. The task was: "Based on the difficulty levels in answering previous questions, please provide your preference to the visualization techniques. A score of 5 means the most preferred and 1 means the least preferred." On average, the double layer was considered as the most preferred and HARD was the least preferred.

The evaluation demonstrated that researchers preferred non-uniformed DDS because they can display more subtle variation in the data. Table I listed the score of Tasks 2 to 5. The results indicated that the proposed technique is in the first rank for the task of APD and ENS. The DIE' score of the proposed method is slightly lower than the score of the double layer, but it is significantly better than the scores of the other techniques.

However, the multilayer did not gain a very good score on the task of OA. The feedback of the researchers indicated that the gap among the sampling pixels impacts the attitude of the viewers since the gap blurs the appearance of an image. Based on the feedback of the researchers, the luminance of layers will be improved by using some lighting strategies. In addition, more user-friendly graphic user interface will be designed to make the multilayer visualization more widely evaluated in the future.

VII. CONCLUSION

This paper presents the use of a feature-driven multilayer scheme to visualize hyperspectral image data. It is based on the linear mixture analysis and takes advantage of the fully constrained mixed-pixel classification. The proposed approach automatically analyzes the spatial distribution and importance of each type of endmembers and then chooses a proper technique to visualize it. It enhances the visibility of anomalous

and low-probability materials. Moreover, it still maintains the capability of visualizing the widely distributed endmembers and the detailed composition at the subpixel level.

Unlike the traditional side-by-side grayscale displays or the sequential-in-time displays, the proposed technique visualizes all of the classification maps for endmembers in a single textured image. It significantly improves the comprehension of the spatial relationship among these collocated endmembers.

Compared to other existing hyperspectral visualization techniques, which mostly visualize hyperspectral imagery as one color image and cannot provide the precise composition at the subpixel level, the embedded pie-chart layer in the multilayer visualization technique provides the precise pixel composition. This is particularly useful when a small region is of great interest. For example, it is feasible to estimate the size of small objects such as invasive species or military targets based on material abundance within a pixel. The anomaly layer highlights the anomalous pixels such as small targets, which can greatly facilitate target detection. The DDS layer displays the widely distributed endmembers such as background materials. The DDS non-uniform sampling can reflect the subtle spatial variation in endmember distribution. The oriented silver layer further emphasizes the distribution of important target materials.

Furthermore, the interactive operation allows viewers to select/deselect endmembers. This operation provides the ability for viewers to investigate individual endmembers or to compare two or more endmembers at the same time. This interaction is lacking in existing visualization techniques. We believe such a synergy can greatly enhance the presentation of the abundant information in hyperspectral imagery at both macro and micro scales and can help researchers efficiently analyze hyperspectral images.

REFERENCES

[1] T. M. Lillesand, R. W. Kiefer, and J. W. Chipman, *Remote Sensing and Image Interpretation*, 5th ed. Hoboken, NJ: Wiley, 2003

[2] P. K. Robertson and J. F. O'Callaghan, "The application of perceptual color spaces to the display of remotely sensed imagery," *IEEE Trans. Geosci. Remote Sens.*, vol. 26, no. 1, pp. 49–59, Jan. 1988.

[3] J. M. Durand and Y. H. Kerr, "An improved decorrelation method for the efficient display of multispectral data," *IEEE Trans. Geosci. Remote Sens.*, vol. 27, no. 5, pp. 611–619, Sep. 1989.

[4] B. Demir, A. Çelebi, and S. Ertürk, "A low-complexity approach for the color display of hyperspectral remote-sensing images using one-bit-transformation-based band selection," *IEEE Trans. Geosci. Remote Sens.*, vol. 471, pp. 97–105, Jan. 2009.

[5] J. S. Tyo, A. Konsolakis, D. I. Diersen, and R. C. Olsen, "Principal components-based display strategy for spectral imagery," *IEEE Trans. Geosci. Remote Sens.*, vol. 41, no. 3, pp. 708–718, Mar. 2003.

[6] V. Tsagaris, V. Anastassopoulos, and G. A. Lampropoulos, "Fusion of hyperspectral data using segmented PCT for color representation and classification," *IEEE Trans. Geosci. Remote Sens.*, vol. 43, no. 10, pp. 2365–2375, Oct. 2005.

[7] A. A. Green, M. Berman, P. Switzer, and M. D. Craig, "A transformation for ordering multispectral data in terms of image quality with implications for noise removal," *IEEE Trans. Geosci. Remote Sens.*, vol. 26, no. 1, pp. 65–74, Jan. 1988.

[8] S. Cai, Q. Du, R. Moorhead, M. J. Mohammadi-Aragh, and D. Irby, "Noise-adjusted principal component analysis for hyperspectral remotely sensed imagery visualization," in *Proc. IEEE Vis. Conf. (Compendium)*, 2005, pp. 119–120.

[9] Q. Du, N. Raksuntorn, S. Cai, and R. J. Moorhead, "Color display for hyperspectral imagery," *IEEE Trans. Geosci. Remote Sens.*, vol. 46, no. 6, pp. 1858–1866, Jun. 2008.

[10] N. P. Jacobson and M. R. Gupta, "Design goals and solutions for display of hyperspectral images," *IEEE Trans. Geosci. Remote Sens.*, vol. 43, no. 11, pp. 2684–2693, Nov. 2005.

[11] N. P. Jacobson, M. R. Gupta, and J. B. Cole, "Linear fusion of image sets for display," *IEEE Trans. Geosci. Remote Sens.*, vol. 45, no. 10, pp. 3277–3288, Oct. 2007.

[12] M. Cui, A. Razdan, J. Hu, and P. Wonka, "Interactive hyperspectral image visualization using convex optimization," *IEEE Trans. Geosci. Remote Sens.*, vol. 47, no. 6, pp. 1673–1684, Jun. 2009.

[13] A. Marcal, "Automatic color indexing of hierarchically structured classified images," in *Proc. IEEE Geosci. Remote Sens. Symp.*, 2005, vol. 7, pp. 4976–4979.

[14] D. C. Heinz and C.-I. Chang, "Fully constrained least squares linear spectral mixture analysis method for material quantification in hyperspectral imagery," *IEEE Trans. Geosci. Remote Sens.*, vol. 39, no. 3, pp. 529–545, Mar. 2001.

[15] D. M. Rogge, B. Rivard, J. Zhang, and J. Feng, "Iterative spectral unmixing for optimizing per-pixel endmember sets," *IEEE Trans. Geosci. Remote Sens.*, vol. 44, no. 12, pp. 3725–3736, Dec. 2006.

[16] R. Wessels, M. Buchheit, and A. Espesset, "The development of a high performance, high volume distributed hyperspectral processor and display system," in *Proc. IEEE Geosci. Remote Sens. Symp.*, 2002, vol. 4, pp. 2519–2521.

[17] R. M. Kirby, H. Marmanis, and D. H. Laidlaw, "Visualizing multivalued data from 2D incompressible flows using concepts from painting," in *Proc. IEEE Vis. Conf.*, 1999, pp. 333–340.

[18] C. Forsell, S. Seipel, and M. Lind, "Simple 3D glyphs for spatial multivariate data," in *Proc. IEEE Symp. Inf. Vis.*, 2005, pp. 119–124.

[19] A. A. Bokinsky, "Multivariate data visualization with data-driven spots," Ph.D. dissertation, Univ. North Carolina, Chapel Hill, NC, 2003.

[20] R. Crawfis, "New techniques for the scientific visualization of three-dimensional multi-variate and vector fields," Ph.D. dissertation, Univ. California Davis, Davis, CA, 1995.

[21] C. Weigle, W. Emigh, G. Liu, R. Taylor, J. Enns, and C. Healey, "Oriented sliver textures: A technique for local value estimation of multiple scalar fields," in *Proc. Graph. Interface*, 2000, pp. 163–170.

[22] R. Taylor, "Visualizing multiple fields on the same surface," *IEEE Comput. Graph. Appl.*, vol. 22, no. 3, pp. 6–10, May/Jun. 2002.

[23] R. J. Vickery, "New visualization techniques for multi-dimensional variables in complex physical domains," Ph.D. dissertation, Mississippi State Univ., Starkville, MS, 2003.

[24] C. G. Healey, "Effective visualization of large multidimensional datasets," Ph.D. dissertation, Univ. British Columbia, Vancouver, BC, Canada, 1996.

[25] C. G. Healey, S. Kocherlakota, V. Rao, R. Mehta, and R. S. Amant, "Visual perception and mixed-initiative interaction for assisted visualization design," *IEEE Trans. Vis. Comput. Graphics*, vol. 14, no. 2, pp. 396–411, Mar./Apr. 2008.

[26] T. Urness, V. Interrante, E. Longmire, I. Marusic, S. O'Neill, and T. W. Jones, "Strategies for the visualization of multiple 2d vector fields," *IEEE Comput. Graph. Appl.*, vol. 26, no. 4, pp. 74–82, Jul./Aug. 2006.

[27] S. Cai, Q. Du, and R. J. Moorhead, "Hyperspectral imagery visualization using double layers," *IEEE Trans. Geosci. Remote Sens.*, vol. 45, no. 10, pp. 3028–3036, Oct. 2007.

[28] J. B. Adams, M. O. Smith, and P. E. Johnson, "Spectral mixture modelling: A new analysis of rock and soil types at the Viking Lander 1 site," *J. Geophys. Res.*, vol. 91, pp. 8098–8112, 1985.

[29] C. M. Schweik and G. M. Green, "The use of spectral mixture analysis to study human incentives, actions, and environmental outcomes," *Social Sci. Comput. Rev.*, vol. 17, no. 1, pp. 40–63, 1999.

[30] F. A. Kruse, A. B. Lefkoff, J. W. Boardman, K. B. Heidebrecht, A. T. Shapiro, J. P. Barloon, and A. F. H. Goetz, "The spectral image processing system (SIPS)—Interactive visualization and analysis of imaging spectrometer data," *Remote Sens. Environ.*, vol. 44, no. 2/3, pp. 145–163, May/Jun. 1993.

[31] J. C. Harsanyi and C.-I. Chang, "Hyperspectral image classification and dimensionality reduction: An orthogonal subspace projection approach," *IEEE Trans. Geosci. Remote Sens.*, vol. 32, no. 4, pp. 779–785, Jul. 1994.

[32] M. P. Eckert and A. P. Bradley, "Perceptual quality metrics applied to still image compression," *Signal Process.*, vol. 70, no. 3, pp. 177–200, Nov. 1998.

[33] A. Toet and M. P. Lucassen, "A new universal colour image fidelity metric," *Displays*, vol. 24, no. 4/5, pp. 197–207, Dec. 2003.

[34] V. Tsagaris and V. Anastassopoulos, "Assessing information content in color image," *J. Electron. Imaging*, vol. 14, no. 4, p. 043 007, 2005.

[35] A. S. Bair, D. H. House, and C. Ware, "Texturing of layered surfaces for optimal viewing," *IEEE Trans. Vis. Comput. Graphics*, vol. 12, no. 5, pp. 1125–1132, Sep./Oct. 2006.

[36] D. Acevedo and D. Laidlaw, "Subjective quantification of perceptual interactions among some 2D scientific visualization methods," *IEEE Trans. Vis. Comput. Graphics*, vol. 12, no. 5, pp. 1133–1140, Sep./Oct. 2006.
[37] M. O. Ward and K. J. Theroux, "Perceptual benchmarking for multivariate data visualization," in *Proc. IEEE Vis. Conf.*, 1997, pp. 314–321.
[38] R. Kosara, C. G. Healey, W. Interrante, D. H. Laidlaw, and C. Ware "User studies: Why, how, and when?" *IEEE Comput. Graph. Appl.*, vol. 23, no. 4pp. 20–25, Jul./Aug. 2003
[39] S. Cai, "Hyperspectral image visualization by using double and multiple layers," Ph.D. dissertation, Mississippi State Univ., MS, 2008.

Shangshu Cai (S'06–M'09) received the B.S. and M.S. degrees in electrical engineering (Special Class for the Gifted Young) from the University of Science and Technology of China, Hefei, China, in 2000 and 2003, respectively, and the Ph.D. degree in electrical engineering from Mississippi State University, Mississippi State, in 2009.

He is currently a Postdoctoral Researcher with the Center for Risk Studies and Safety, University of California, Santa Barbara. His research interests include scientific visualization, high-dimensional data visualization, hyperspectral image displaying, and image processing.

Qian Du (S'98–M'00–SM'05) received the Ph.D. degree in electrical engineering from the University of Maryland, Baltimore, in 2000.

From 2000 to 2004, she was with the Department of Electrical Engineering and Computer Science, Texas A&M University, Kingsville. In Fall 2004, she joined the Department of Electrical and Computer Engineering, Mississippi State University, Mississippi State, where she is currently an Associate Professor. Her research interests include remote sensing image analysis, pattern classification, data compression, and neural networks.

Dr. Du currently serves as Co-Chair for the Data Fusion Technical Committee of the IEEE Geoscience and Remote Sensing Society. She also serves as a Guest Editor for the special issue on Spectral Unmixing of Remotely Sensed Data in the IEEE TRANSACTIONS ON GEOSCIENCE AND REMOTE SENSING and Guest Editor for the special issue on High Performance Computing in Earth Observation and Remote Sensing in the IEEE JOURNAL OF SELECTED TOPICS IN APPLIED EARTH OBSERVATIONS AND REMOTE SENSING. She is a member of SPIE, ASPRS, and ASEE.

Robert J. Moorhead, II (S'81–M'85–SM'92) received the B.S.E.E. degree from Geneva College, Beaver Falls, PA, in 1980, and the M.S.E.E. and Ph.D. degrees in electrical engineering from North Carolina State University, Raleigh, in 1982 and 1985, respectively.

He is currently a Professor with the Department of Electrical and Computer Engineering and the Director of the Geosystems Research Institute, Mississippi State University, Mississippi State. He was previously a Research Staff Member at the IBM T. J. Watson Research Center, Yorktown Heights, NY. His current research interests include computationally demanding visualization and analysis issues. He has previously conducted research in computer communications and image/video coding. He has published more than 100 papers.